



## Comparison of elemental resolved non-confined and restricted electrochemical degradation of nickel base alloys

Dominik Dworschak<sup>a</sup>, Hsiu-Wei Cheng<sup>a</sup>, Ching-Shun Ku<sup>b</sup>, Ching-Yu Chiang<sup>b</sup>, Chia-Hsien Lin<sup>b</sup>, Markus Valtiner<sup>a,\*</sup>

<sup>a</sup> Vienna University of Technology, Institute of Applied Physics, Wiedner Hauptstrasse 8-10, A-1040, Vienna, Austria

<sup>b</sup> Materials Science Group, National Synchrotron Radiation Research Center, Taiwan

### ARTICLE INFO

#### Keywords:

Nickel base alloys  
ICP-MS  
Restricted (confined) corrosion  
Localized corrosion  
Oxide breakdown  
Synchrotron-XRF

### ABSTRACT

Passive film properties of nickel base alloys (NBAs) have been studied extensively, yet elemental resolved dissolution currents under corrosive conditions are less well studied. Here, we compare elemental dissolution currents during anodic polarisation and repassivation under crevice and freely-exposed conditions for various NBAs using an ICP-MS flow-cell approach. With a new sample design we can track communication of a crevice environment with the electrolyte, providing insight into crevice solution chemistry and solubility of passive film-forming elements. Data indicates Mo can only form stable precipitate layers under openly corroding conditions. Local elemental depletion was further examined by XPS and nanometer resolved XRF.

### 1. Introduction

Compared to stainless steels nickel base alloys (NBAs) are considerably more corrosion resistant making them a preferred industrial choice in demanding environments, including chemical and food processing, aerospace as well as energy applications. [1–4] NBAs are typically alloyed with >10 % chromium and 1–5 % molybdenum which are key alloying elements for providing an excellent corrosion resistance in extreme environments. [5–8] The pronounced corrosion resistance in anodic and acidic environments suggests the formation of a very stable and well adhering passivating thin film, which is formed and/or stabilized mainly by these alloying elements. [8–11] It has been suggested that molybdenum and chromium may segregate to the alloy surface [6, 9,11–13].

The thickness of the passive films is estimated at about 2 nm [6,14] and the chromium content is known to strongly influence the breakdown of the passive film. This suggests a key role of chromium in the passive film chemistry, formation kinetics and stability. [9,14] The mechanism of molybdenum inhibition is less well understood. Increasing molybdenum content results in lower passive currents, and it was suggested that  $MoO_4^{2-}$  ions (molybdates) accumulate at the outer interface of the passive film. [12] This may stabilize the passive film against chloride ingress and hence dissolution, resulting in lower corrosive currents. [6, 15]

It was further suggested that molybdenum forms insoluble molybdate species after anodic dissolution from the matrix, building up passivating precipitate films which in turn lowers anodic dissolution rates. [13]

Jakupi et al. [16] suggested that molybdenum may accumulate at defect sites, which may also trigger lower anodic dissolution rates there.

While passive films and passivity have been studied extensively for NBAs, the elemental resolved dissolution during and after breakdown of the oxide, specifically under crevice and pitting conditions, is less well studied. Material dissolution is a central aspect of an ongoing localized corrosion, and industrial cleaning procedures involve pickling, where a complete oxide breakdown is desired, which is particularly demanding for NBAs. [17]

Recent studies by Ogle et al. [13] investigated the transpassive dissolution in high salt environments, and NBA passivation in acidic solutions [18] using spectroelectrochemistry in flow-cells coupled to ICP-OES analysis.

Here, we use a similar approach in a newly designed ICP-MS flow cell [19,20] shown in Fig. 1a. This cell allows us to measure and compare elemental dissolution rates and faradaic currents under crevice and pitting conditions (see Fig. 1b/c), depending on the sample design, respectively. Similar to classic flow-cell designs a crevice is formed with the sealing O-ring, if a bulk sample (type 1) is mounted. Fig. 1b also shows a finite element simulated concentration profile of corroding

\* Corresponding author.

E-mail address: [markus.valtiner@tuwien.ac.at](mailto:markus.valtiner@tuwien.ac.at) (M. Valtiner).

species in the flowing electrolyte, demonstrating significant dissolution in the crevice region under the O-ring. In contrast, as shown in Fig. 1c, an embedded sample (type 2) can be mounted without crevice formation under the O-ring. The well adhering glue limits crevice formation at the embedded glue/sample edge during experimental duration, as demonstrated by comparison of the visual corrosive damage after experiments (Fig. 1c). Also, finite element simulations, shown as insets, indicate that the dissolving species originate from the exposed area. The flow is also guided well into the exit for both sample settings, ensuring limited convective broadening of the ICP-MS signal. This is ensured by the design of the flow channels, which enter and exit as circular openings between O-ring and a PTFE stamp. This ensures a stable channel height and laminar flow.

Using this setup, we study the elemental dissolution behaviour of a series of commercial and model NBAs under crevice and non-crevice conditions. The alloy compositions and abbreviations used in this work are given in Table 1. The compositions were selected for evaluating the influence of the total chromium content (5% and 16% Cr) and the impact of trace/minor amounts of molybdenum (1% Mo) on initial corrosion and subsequent repassivation.

## 2. Results

Here, we first quantify elemental dissolution currents  $i_{MS}$  during polarisation at different anodic polarisation for crevice and non-crevice type samples in the ICP-MS (see again Fig. 1)). We characterize extended corrosive dissolution and the subsequent repassivation of the materials, to obtain insight into the crevice chemistry. As a side note, in this work we do not study freely corroding crevices under OCP conditions, we rather accelerate the degradation reaction by application of anodic potentials, in the transpassive regime.

We then further characterize the surface chemistry of corroded and repassivated alloys with X-ray photoelectron spectroscopy (XPS) and discuss the passivating film chemistry and structure before and after corrosive dissolution. Finally, high-resolution X-ray fluorescence spectroscopy was performed on corroded samples, to further visualize local elemental surface depletion at corroding sites.

### 2.1. Anodic polarisation and elemental resolved dissolution

Fig. 2 displays representative data of elemental dissolution currents  $i_{MS}$  recorded during 40 min active corrosion with a type 1 (electrochemically triggered degradation under confined conditions) and type 2 (open area electrochemical degradation) samples at  $\varphi_{TP} = 1.0$  V for,  $Ni_{86}Cr_5Fe_9$  (Cr5), Alloy 600, and  $Ni_{74}Cr_{16}Fe_9Mo$  in aerated 1 mM NaCl solution at unbuffered pH of 7, respectively.

First, based on absolute dissolution currents, these three samples indicate increasing corrosion resistance from  $Cr5 < Mo1 \sim Alloy\ 600$  for the electrochemically triggered degradation under confined conditions (CC), and  $Cr5 < Alloy\ 600 < Mo1$  for open area corrosion.

Second, under crevice condition (Fig. 2 a–c), stepping from 0.2 V to 1.0 V, *i.e.* results in an immediate and steep increase of nickel dissolution

**Table 1**

Bulk composition (weight ratios) and abbreviations for all NBAs used.

Alloy composition	abbreviation	Ni	Cr	Fe	Mo	Minor components
$Ni_{86}Cr_5Fe_9$	Cr5	86	5	9	–	–
$Ni_{75}Cr_{16}Fe_9$	600	72	15.5	8	–	Mn(1) Si(0.5)
$Ni_{74}Cr_{16}Fe_9Mo$	Mo1	74	16	9	1	–

rates over more than one order of magnitude for all alloys. Alloys 600 and Mo1 further indicate a peak dissolution of nickel after 30 s, followed by a steady decay of the dissolution rate during ongoing corrosion at 1.0 V. In contrast, for the Cr5 alloy Cr dissolution shortly plateaus after 30 s, and after 90 s the dissolution rate of all elements increases further. Fig. 2a also shows that for Cr5 the second increase of  $i_{MS(Ni)}$  after 90 s is accompanied by a steep increase of the iron dissolution rate over more than one order of magnitude. The dissolution ratios ( $D_R$ ) after 40 min active corrosion shown in Fig. 3 indicate that Cr5 reaches close to bulk dissolution ratios, while Alloy 600 and Mo1 exhibit comparatively higher Cr, as well as considerably enhanced Mo dissolution ratios, respectively, with a clearly retarded Fe dissolution under crevice conditions.

Under openly corroding conditions of embedded samples (Fig. 2d–f), stepping from 0.2 V to 1.0 V, *i.e.* indicates a similar pattern with a very steep increase of Ni-dissolution. In contrast to the CC type and shown in Fig. 3, open corrosion establishes a near bulk-ratio dissolution after 40 min, with moderately higher Ni, and hence lower Fe and Cr dissolution rates, compared to the bulk composition. For the open corrosion we also see that the electrochemical current ( $i_{ec}$ ) is lower compared to measured dissolution current for Cr5 and Alloy 600. In contrast, Mo1 shows a generally very low corrosion rate, with a second increase of rates after an initial 2–3 min of anodic corrosion.

### 2.2. Repassivation

Fig. 4 compares elemental dissolution currents for all alloys and sample types during repassivation after 5 and 40 min of corrosive polarisation, respectively.

Due to diffusion broadening [21] all samples show, that the dissolution currents for all alloys drop to a lower base level within 60–100 seconds after stepping into the repassivating region at  $\varphi_1 = 0.2$  V. This results from the retention time of the dissolved material in the tubes between the electrochemical cell and the detection in the ICP-MS.

*Type 1 samples:* Fig. 4a–c shows type 1 samples, indicating that the base level for the Cr5 alloy is almost half an order of magnitude higher compared to alloys 600 and Mo1. This is in line with the polarisation curves, shown in Fig. S1. For Cr5 the passive current level also depends on the transpassive polarisation time. After 5 min of the resulting passive dissolution the current of all elements is about 20–30% higher compared to longer polarisation times. In contrast, both alloy 600 and alloy Mo1 show no pronounced difference of dissolution currents after 5 or 40 min anodic corrosion followed by repassivation.

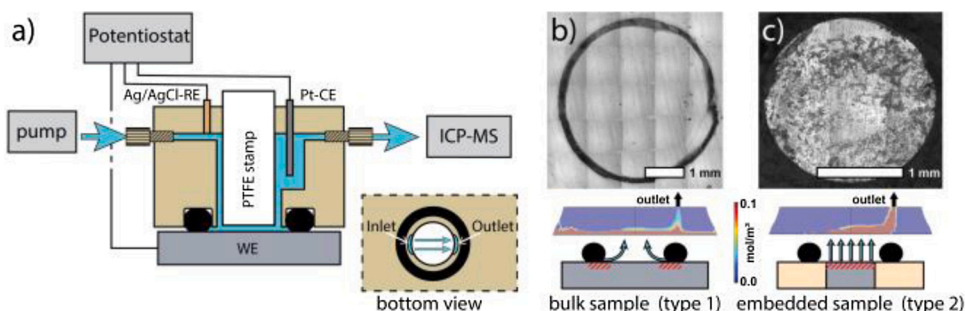


**Fig. 1.** a) Schematic of the flow cell used. A PTFE cylinder is used for establishing laminar flow across the working electrode. The counter electrode (Pt) is placed up-stream and the reference electrode (Ag|AgCl) is placed down-stream to avoid contamination of the WE. Standard HPLC fittings are used for all tubings. Corrosion patterns for different types of experiments are shown schematically and as microscope pictures for b) crevice corrosion and c) embedded samples, as well as a finite element method simulation (see methods) of the concentration distribution after 1.5 s of material release at the electrode surface.

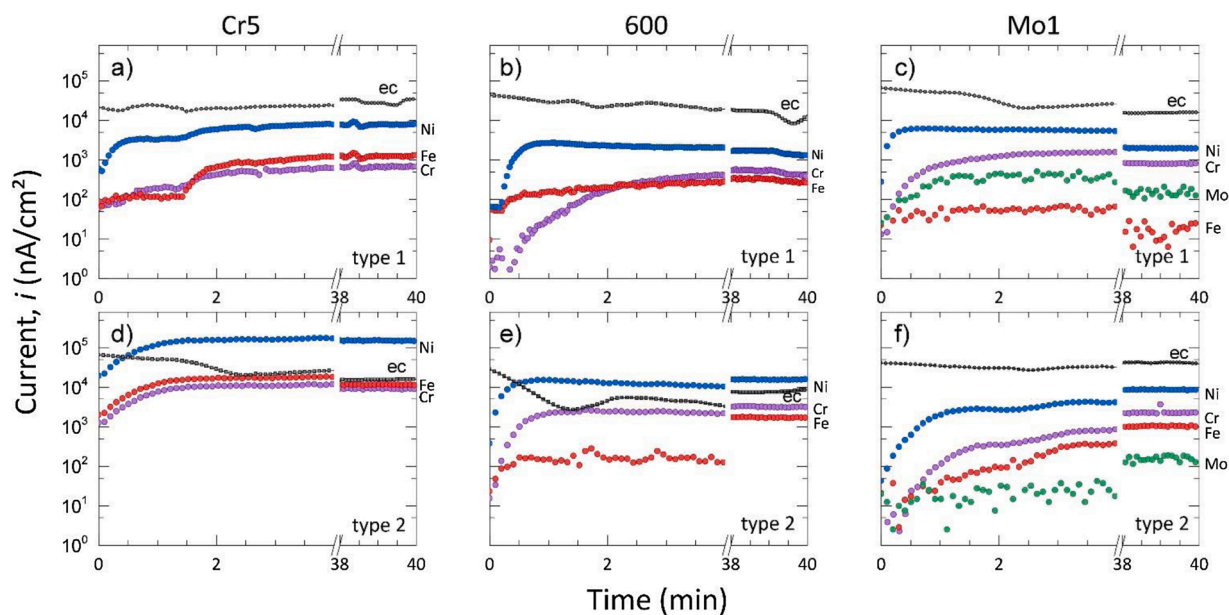


Fig. 2. Comparison of anodic dissolution at bulk pH = 7 in 1 mM NaCl of Cr5, alloy 600 and Mo1. Multiple repetitive measurements provided similar quantitative results. Rates are normalized to the electrode area, which is estimated at the circumference and width of the observed crevice for type 1, and the embedded area for type 2 samples.

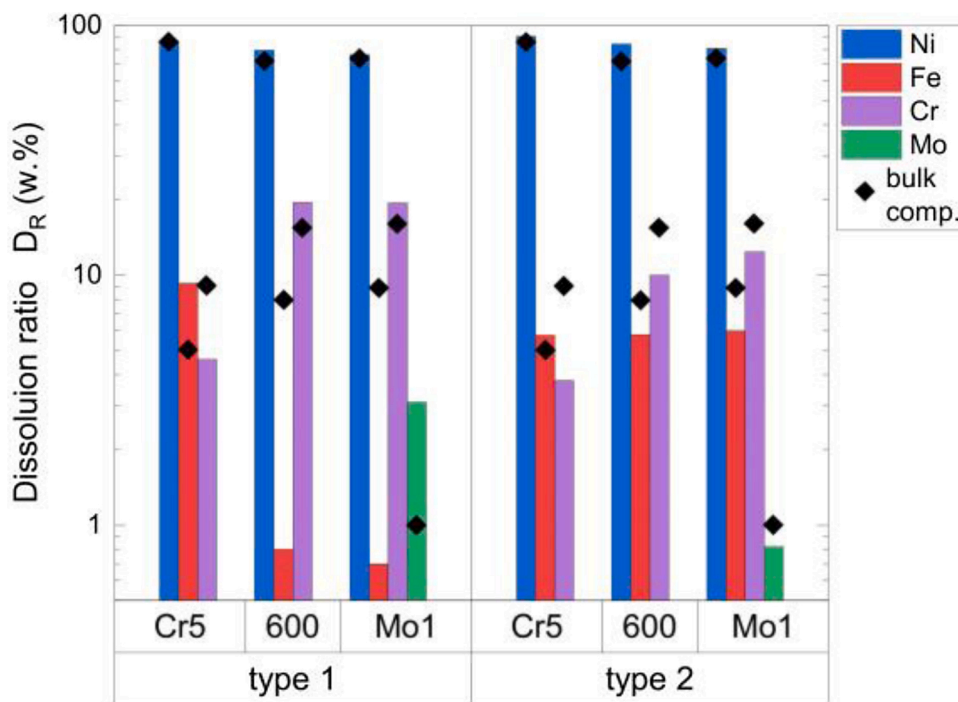
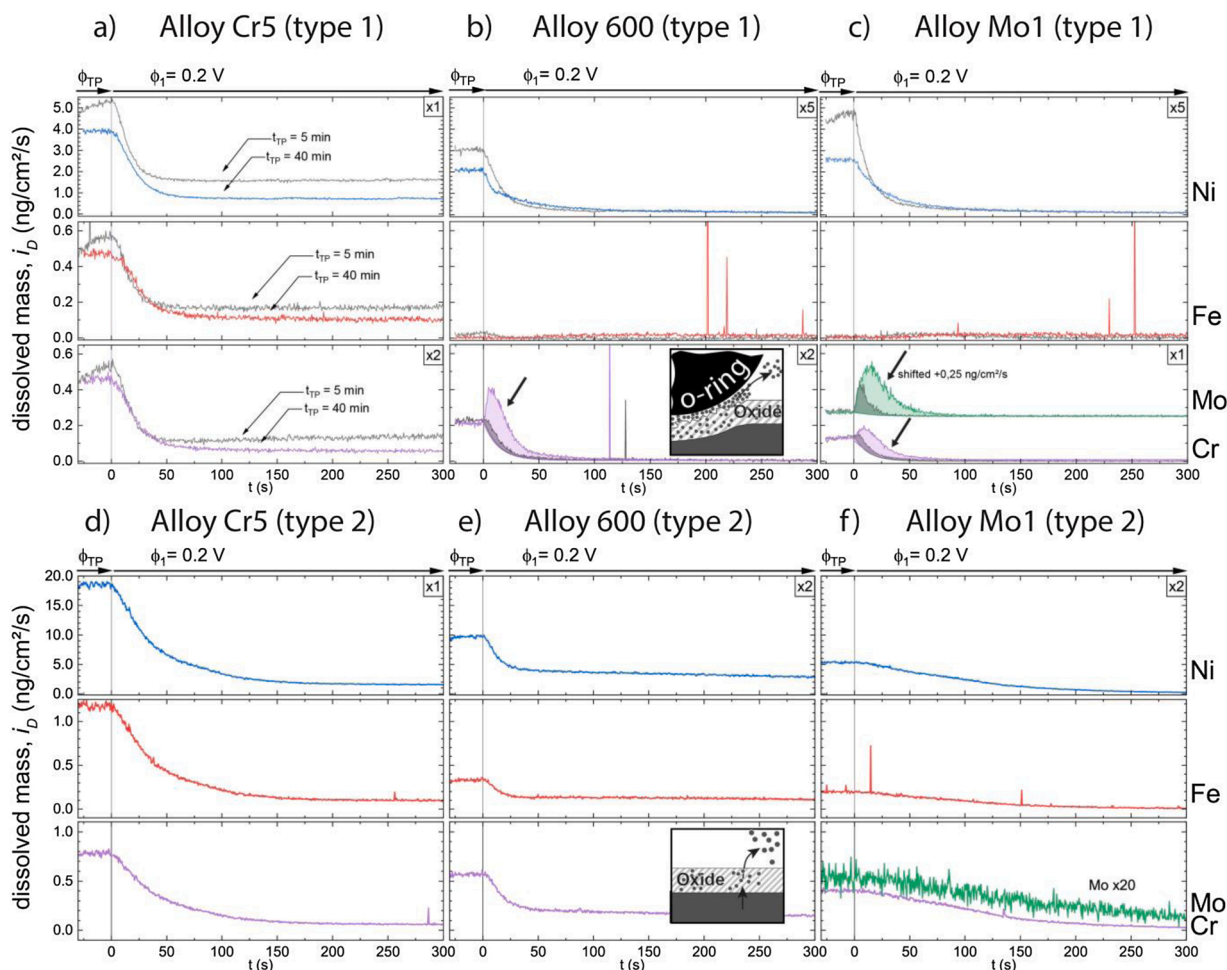


Fig. 3. Extended anodic dissolution ratios  $D_R$  for all  $n$  elements after 40 min of corrosion for all NBAs under different conditions of anodic polarisation as  $D_R = \frac{i_{ms}(j)}{\sum_{j=1}^n i_{ms}(j)}$ . Bulk values are indicated by black diamonds.

During repassivation the iron dissolution remains negligible for alloys 600 and Mo1, and remains at a significantly higher level for the Cr5 alloys.

In contrast to the Cr5 alloy both, alloys 600 and Mo1, indicate a significant initial peak of the dissolution rate of Cr and Mo during repassivation (marked by arrow), which increases with the time of preceding anodic polarisation. The dissolution rates for Cr and Mo peaks are considerably above the value measured during corrosive dissolution, indicating a significant material release during repassivation.

Fig. S2 compares the integrated amount of dissolved chromium and molybdenum during repassivation as a function of the transpassive polarisation time. Data indicates a saturation after about 20 min of transpassive polarisation. Furthermore, comparing the integrated Cr and Mo dissolution currents for alloys Mo1 and 600 (Fig. S2) during repassivation indicates that the Mo content in Mo1 results in a smaller dissolution current for the Cr during repassivation for up to 20 min of corrosive polarisation. During this initial period a considerably larger amount of Mo peak dissolution occurs during repassivation, while only



**Fig. 4.** Elemental dissolution rates during repassivation after 5 and 40 min polarisation in the anodic region (grey: 5 min, colored: 40 min). a)+c)  $\text{Ni}_{86}\text{Cr}_5\text{Fe}_9$  b)+d)  $\text{Ni}_{75}\text{Cr}_{16}\text{Fe}_9$  and c)+e)  $\text{Ni}_{74}\text{Cr}_{16}\text{Fe}_9\text{Mo}$ . Notice: For b) and c) Ni-rates are multiplied by 5 for e) and f) by 2, and Cr-rates of a) and b) are multiplied by 2 to be at scale for all alloys, respectively. a)-c) show samples with crevice (type 1). Insets show schematically the mechanism of dissolution for type 1 & 2.

limited chromium dissolution emerges. After 20 min of corrosive dissolution the dissolved amount of chromium is again similar compared to alloy 600 that is polarised at 1.0 V.

**Type 2 samples:** For type 2 samples shown in Fig. 4d-f no such peaks were observed, and for Cr5 and Alloy 600 a decay of the dissolution currents consistent with diffusion broadening was observed. In contrast, Mo1 shows a prolonged dissolution time for all elements during repassivation.

### 2.3. Surface characterization - XPS

XPS was further used to compare passive films formed during passivation and after corrosion and repassivation. Therefore spectra were collected at openly corroded and at crevice corroded regions, using a small spot XPS. For these XPS measurements the surfaces were pulled out from the electrolyte at the given potential and they were washed afterwards with minute amounts of MilliQ water, to avoid significant changes of the surface chemistry due to washing (see experimental details for more information). We want to emphasize, that this procedure allows us to closely resemble, or "freeze", [22] the conditions in the electrolyte. But clearly, *ex-situ* XPS is only an approximation for the state during active aqueous degradation. In future work, one may expect further insight from high pressure XPS. [23,24]

The full set of core level spectra for all alloys and elements are shown in the supporting information for all materials studied for openly corroded areas (Fig. S3-S5), and crevice corroded areas (Figs. S6-S7)

respectively. Peak fitting was applied as shown in the spectra, and resulting XPS surface ratios for metallic and oxide components of fitted compounds are summarized in Fig. 5a.

Survey spectra indicated no further elements other than atmospheric carbon. We first summarize the results of the spectra for the major elements, while Mo is discussed separately, as it indicates most pronounced differences.

#### 2.3.1. Cr, Fe, Ni spectra after non-crevice passivation

After 40 min of open crevice free passive polarisation at 0.2 V 600 and Mo1 indicate a  $\text{Cr}_2\text{O}_3$  and  $\text{Fe(III)}$  enriched passive film, while oxidized Ni appears to be insignificant, and mostly metallic Ni is observed. In contrast, Cr5 shows a considerably more Ni-rich (60 %) surface and the Cr content in the passive film is still two-fold above bulk level concentration.

#### 2.3.2. Cr, Fe, Ni spectra after open corrosion

XPS spectra recorded after corrosion (Figs. S3-S5) indicate significant differences of the passive film content. First, the Ni-signal indicates a more pronounced oxide/hydroxide component after reprecipitation, which is in line with a reprecipitated outer layer of nickel oxide/hydroxide. Also, the metallic signals for both alloy 600 and Cr5 show a considerably lower intensity of metallic Cr and Fe relative to the oxidized species, indicating a thicker passive film.

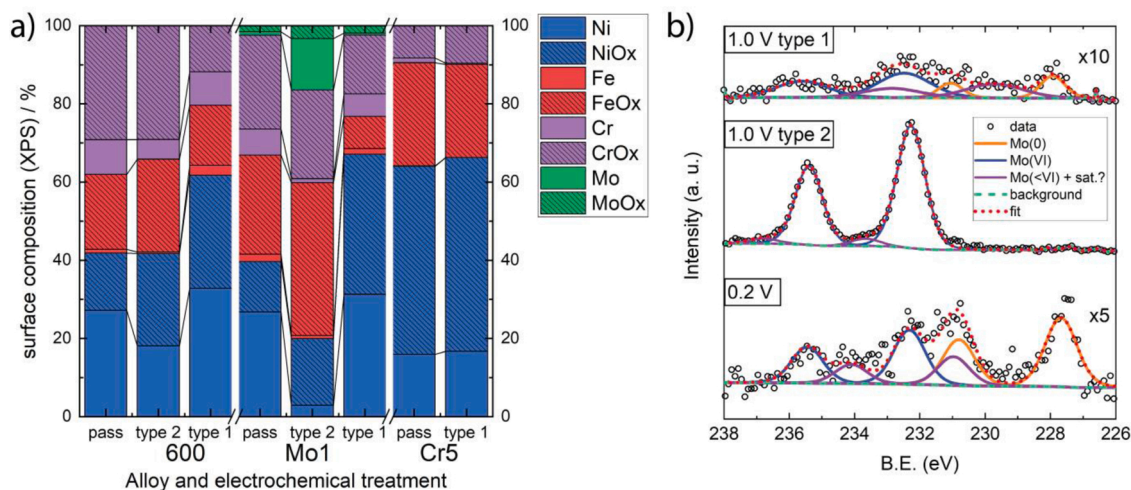


**Fig. 5.** a) Surface composition of the alloys according to XPS analysis. Type 1 and 2 were polarised at 1.0 V for 40 min, pass indicates passivation at 0.2 V for 40 min. Type 1 is measured at the area of the crevice, type 2 represents the data taken from spots in the inner part of the metal sample. b) Molybdenum 3p core level spectra after 40 min of polarisation in the (bottom) passive regime at 0.2 V, and (top) the anodic regime at 1.0 V for type 1 and type 2 polarisation. (c.f. text for details).

### 2.3.3. Cr, Fe, Ni spectra after crevice corrosion

Spectra under crevice condition (Figs. S6-S7) clearly indicate a thinner oxide in the crevice corrosion. Specifically, relative comparison of the metallic and the oxide peaks indicates a relatively higher metal signal for all alloys. Further, Ni(II) shows no hydroxide signals for all alloys.

### 2.3.4. Comparison of Mo spectra

As shown in Fig. 5b, for Mo1 the elemental ratios of the Mo oxides strongly differ for the openly exposed, crevice and passive film surface chemistry.

First for open non-crevice corrosion (type 2), after passivation molybdenum at 0.2 V is chemically present as Mo(VI) and lower oxidized species Mo(<VI). Also, metallic Mo is clearly detectable indicating a thin passive film.

Second, and in contrast, Mo core level spectra in Fig. 5 after corrosion at 1.0 V and repassivation indicate a fully oxidized and highly

enriched Mo(VI) species in the passive film. The data indicates a nearly exclusive Mo(VI) content, with a minor (~ 6%) possibly defect (e.g. oxygen interstitial) related peak at even higher binding energies after transpassive dissolution and subsequent repassivation. This small peak is shifted to very high binding energies, which in our view supports an interpretation of an interstitial site, which is highly coordinated by lattice oxygen (defect). Other secondary effects such as shake ups are unlikely in this case, as the highly oxidized form is expected to be diamagnetic. [25] The total Mo content in this passive film is at 7–8 %, which is considerably above the 1% bulk concentration. This indicates a thick molybdate precipitate overlayer, which is also consistent with the disappearance of the metallic Mo peak, and significantly weaker metallic peaks in all other elemental spectra (Fig. S4).

Finally, the spectra in the crevice corroded area (type 1, 1.0 V) indicate fully oxidized species, and only minor lower oxidation states (in the noise limit). In general, the considerably smaller signal levels again indicate a lower film thickness, in particular considering that the

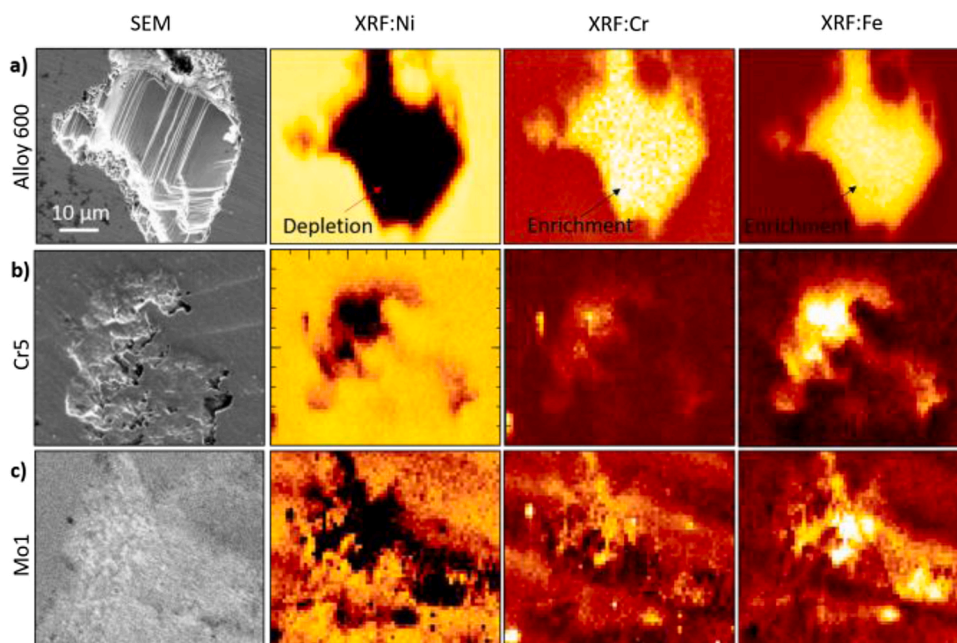


**Fig. 6.** High resolution XRF characterisation of corroded areas of a) Alloy 600, b) Cr5 and b) Mo1 alloys. The left column shows an SEM image, followed by a column showing Ni, Cr and Fe depletion/enrichment respectively (cf. text for details).

metallic Mo signal is still visible.

#### 2.4. Nano-XRF/SEM characterization of corroded areas

Fig. 6 shows electron microscopy images and corresponding high resolution (500 nm spatial resolution) XRF elemental mappings for representative areas showing corrosive damage after polarisation in the ICP-MS cell. The elemental mappings show a relative distribution of elements over the probed location (see methods for details), and indicate that nickel depletes locally, while iron and chromium maps indicate a local enrichment compared to bulk level at corroded sites, which is consistent with XPS data. For Mo1 it was not possible to achieve sufficient signal intensity for mapping local changes.

### 3. Discussion and interpretation

#### 3.1. Comparison of anodic corrosion and elemental dissolution under restricted and non-restricted conditions

Our data indicates that we can follow both a freely exposed corrosion of an embedded sample, or preferential confined condition-type degradation (CC) underneath the O-ring using targeted ICP-MS flow cell/sample design concepts. CC establishes a direct communication of the crevice electrolyte with the bulk electrolyte flowing through the ICP-MS flow cell.

First, the open corrosion of type 2 samples results in a preferential dissolution of Ni, while Cr as well as Fe dissolve at ratios below bulk level metal concentrations at both passivating and anodic corrosion conditions. Under passive conditions, at 0.2 V, the Ni-hydroxide and oxide peaks in XPS almost disappear, which is in line with the observed dissolution behaviour in ICP-MS. This suggests, Ni dissolves through an intact chromium oxide layer, and any initially present oxidized Ni species dissolve as well, as expected for a high field mechanism. [26–28] I.e. the potential gradient drives the Nickel dissolution through the formed passive layer. At 1.0 V anodic corrosion we see a preferential and also localized dissolution (see also Fig. 1c photograph after corrosion), which is further evident from the XRF data, which shows depletion of Ni and enrichment of the other alloying elements locally. Localized corrosion is likely triggered by the local breakdown of the passive film. Further, for Mo1 repassivation leads to the formation of an expected passivating Mo (VI)-rich precipitate. This interpretation is consistent with previous work, [13,18] and suggests high oxidation states in the Mo-precipitate formed at 1.0 V. This precipitate dissolves slowly after repassivation, as evidenced by the slow transient ICP-MS dissolution profile of Mo in Fig. 3f. Based on the XPS data, the Mo content of the passive film increases 7-fold compared to the bulk concentration, and the film thickness is above 3–4 nm, but below 10 nm, based on the relative intensities of the metallic signals from underneath the passive film. Under different conditions e.g. Ogle et al. [13] found a similar enrichment of Mo at the interface, as it is also known for Mo-containing stainless steels. [29]

For crevice type samples the ICP-MS repassivation data show two interesting aspects: First, and as discussed above we see clear and time dependent peaks of the Cr and Cr/Mo dissolution, for alloy 600 and Mo1 respectively. These peaks were only found for type 1 samples. Hence, these are clearly related to the communication of the crevice solution with the flowing electrolyte. Upon lowering of the potential, the crevice environment, which established over the extended degradation period, dissipates by peaking, i.e. injecting, the crevice solution into the flowing electrolyte. Hence, the crevice solution at pH 7 base-level unbuffered pH is highly enriched in Cr and Mo containing soluble species, while Fe remains largely insoluble within the crevice. Based on the time dependent evolution of this dissolution peak, shown in Fig. S2, the crevice environment reaches saturation after 20 min of constant polarisation under the applied conditions. [24] The here studied approach deviates from realistic crevice corrosion since an external potential is applied, that likely results in an overestimation of the exchanged currents. [30]

Nevertheless the processes taking place in the crevice environment are comparable. The here reported enrichment in soluble species in the crevice is also found for crevice corrosion. [31,32] Interestingly, for Mo1 data indicates a delayed Cr dissolution, while Mo preferentially dissolves initially. After 20 min, similarly, a saturation level is reached.

Further the observed Fe retardation for both alloys indicates that the crevice is enriched with iron oxide, while Cr-oxide and Mo have lower effective protection levels in the crevice. The resulting oxide/ transient protection layer is non-well adhering and does not passivate the active crevice surface well. This is consistent with 1) the observed current spikes in the Fe signal. The observed spikes indicate nano-to-micro level Fe-oxide detachment from the repassivating areas, and 2) XPS of the crevice region also indicates Fe enrichment, and overall thinner oxide.

When comparing the surface composition of non-confined with the crevice corroded samples, data clearly suggests an acidification of the crevice area, which drives localized corrosion, while inhibiting passive film formation. [31,33–35] For the openly corroding samples, a similar breakdown of the oxides appears locally, as can be seen from the visual corrosive damage, which showed localized attacks. The fact that the dissolution current of Cr5 and alloy 600 was consistently higher compared to the electrochemical current (Fig. 2d/e) further supports that oxygen reduction (from aerated solutions) occurred simultaneously at the bare metal/solution interface, indicating a localized decomposition of the passive film.

In contrast, for Mo1 both the ICP-MS data and the XPS data presented here further confirm the formation of a passivating layer of fully oxidized molybdenum oxide at 0.2 V (see again XPS), which is still quite stable at 1.0 V. Both the increasing Mo dissolution over time during corrosion at 1.0 V (Fig. 2f), and the observed transient extended dissolution during repassivation (Fig. 4f) suggest a solution side based repassivation mechanism (reprecipitation mechanism) of the passive film during corrosion and during step down into the passive region for Mo1. At different conditions, Ogle et al.<sup>13</sup> also observed Mo precipitation based on chemical molybdate dissolution after transpassive polarisation.

This is consistent with current interpretation of the effect of Mo. Precipitation of molybdates passivates the surface for an openly corroding system. [13,36,37]

However, under crevice conditions, we clearly see a lower protective effect, and no pronounced precipitation of molybdates. XPS and ICP-MS data for crevice type samples indicate a lower oxide thickness and soluble molybdate species. Within the crevice region no highly oxidized molybdate based passive film can hence form, probably resulting from the acidification in the crevice and therefore increased solubility of the molbdates. [13]

### 4. Conclusions

In conclusion, we can show that our sample design allows a comparative study of open and crevice type corrosion within the same ICP-MS flow cell. The communication of a crevice environment with the bulk electrolyte can be reproducibly tracked, providing insight into the crevice chemistry. Together with modelling, backtracking the exact chemistry and pH may become possible in the future.

Regarding the characterized systems, our findings are in line with the current understanding of NBA corrosion behaviour, and can be summarized as follows:

- During passivation the passive films are mainly consisting of Fe and Cr oxides, while Ni establishes a passive current by dissolution across the intact passive film.
- Under open corrosion we see a clear preferential dealloying of Ni at localized corroding areas.
- Consistent with ICP-MS dissolution currents, nanometer resolved XRF was utilized to confirm localized selective dissolution of Ni, and enrichment of the other alloying elements.

- The formation of a passive film with >7-8 % MoO<sub>3</sub> confirmed a selective enrichment of Mo after corrosive dissolution and consequent repassivation for Mo1.
- In the crevice region oxides are thinner, and iron oxide enriches significantly, while the other alloying elements, including Cr, dissolve at higher rates and above bulk level concentration in the crevice.
- Under crevice condition Mo(VI) can hence not precipitate an effective protective layer, likely due to the low pH level that establishes in the crevice environment.

## 5. Methods and materials

- a *Chemicals and Materials* Sodium chloride (Carl Roth, p.a.), HNO<sub>3</sub> (VWR Chemicals, Normatom), Milli-Q water (resistivity >18 MΩ·cm, total organic carbon < 4 ppb) was used for making electrolyte solutions. Alloy 600 was obtained from VDM-Metals, and Cr5 and Mo1 were provided by Hauke Springer (MPI f. Eisenforschung, Düsseldorf). For embedded samples a 2 mm diameter cylinder was turned. The removed material was replaced with EPON 1009 F epoxy resin (Hexion). The metal blocks were ground with sand paper of decreasing grain size (from P80 to P2500), then polished with diamond paste down to 0.05 μm. Prior to electrochemical transcritical dissolution at  $\varphi_{TP} = 1.0$  V the metals were preconditioned in-situ in the ICP-MS flow cell by (1) 5 min potentiostatic polarisation at -0.2 V vs OCP, (2) followed by stepping into the passive regime at  $\varphi_1 = 0.2$  V for another 5 min. We also compared results after preconditioning at 1.0 V and subsequent oxidation in the passive regime at 0.2 V and found no quantitative differences.
- b *Inductively Coupled Plasma Mass Spectrometry (ICP-MS)* Measurements were performed using an Agilent 7900 ICP-MS from Agilent Technologies. Calibration was performed with multi-element standard solutions provided by Agilent and Inorganic Ventures. The ICP-MS uses a collision cell with 5 mL/min flow of helium as cell gas. Downstream of the electrochemical cell the analyte was mixed with standard solution. Cobalt was chosen as internal standard due to its similar mass with most of the alloy components. Electrochemical experiments were performed using a home-built flow cell out of PEEK and PTFE inspired by the Ogle- and Mayrhofer designs.<sup>19-21</sup> In the cell design used particular attention was given to the flow profile, so that laminar flow is achieved (confirmed by flow simulations). The exposed electrode area is circular with an sealed with a 3 mm diameter O-ring. Fig. 1 shows the flow-cell ICP-MS coupling used in this work. Pressurized nitrogen was used for pumping to establish a stable and pulsation free laminar flow of the electrolyte. Flow was checked both by an in-flow pressure sensor and by weighing the collected waste electrolyte after ICP-MS. The flow is set to  $6 \pm 0.2$  mg of solution per second. Before each experiment the electrolyte was purged with compressed and filtered air for at least 30 min to guarantee the same concentration of dissolved oxygen. All electrochemical experiments were done using a Ag/AgCl-Electrode as reference and presented data is referenced to that potential.
- c *Optical Microscopy* Optical Microscope images were taken using a μsurf explorer (NanoFocus AG) and analyzed with μsoft metrology software. A 20x magnifying lens was used.
- d *Scanning Electron microscopy (SEM)* SEM imaging was performed at the USTEM facility at Vienna University of Technology, working on a FEI Quanta 250 FEG with a beam energy of 5 keV.
- e *X-ray Photoelectron Spectroscopy (XPS)* XPS Chemical composition and chemical states of the surface were determined using the Axis Supra (Kratos Analytical) spectrometer. No charge neutralization was used. XPS spectra were shifted with respect to adventitious carbon at 284.8 eV. Spectra were taken with a resolution of 0.1 eV and a pass-energy of 160 eV. All spectra were fitted using reference compounds from the NIST database (Ni, Fe, Cr, Mo). [38-41] No positional shifts of the components were necessary to fit the

measured spectra well, except for an 0.2 eV shift for Ni(OH)<sub>2</sub> and 0.5 eV shift for NiO reference components. Elements with unpaired electrons (Cr, Fe) were fitted with fixed multi-peak envelopes. [40, 42] Samples were during active potential application pulled out of electrolyte to 'freeze' the electric double layer. Afterwards they were dried in a N<sub>2</sub> stream.

- f *X-ray fluorescence (XRF)* High resolution X-ray fluorescence (XRF) experiments were performed at the Taiwan Photon Source (TPS) Beamline 21A at the National Synchrotron Radiation Research Center (NSRRC), Taiwan. This beamline is dedicated to white-light nano Laue diffraction for structural analysis and high spatial resolution fluorescence imaging. The spatial resolution can regularly reach 80 × 80 nm at this beamline. In XRF application, the beamline utilizes a pre-shaped Kirkpatrick-Baez mirror pair to focus the Monochromatic X-ray beam with energies 9.6 keV to generate fluorescence signal. XRF was collected by an in-plane detector with a takeoff angle of 7 degree to increase the sensitivity to the surface fluorescence signal. Due to the fact that absolute XRF signal intensity is also influenced by the surface morphology, we normalize the fluorescence imaging and analyze intensity ratio between individual elemental signals as following, revealing relative local variation of elemental ratio on the surface:

$$P_{Me}(\%) = I_{Me} / (I_{Ni} + I_{Cr} + I_{Fe}) \cdot 100 \%$$

The sampling depth of XRF technique is related to the photon energy of fluorescence, which is characteristic for individual elements. A rough estimation of the sampling depth from the XRF energies for Ni, Cr and Fe suggests 2.36, 0.96 and 1.53 μm sampling depths in this sampling geometry.

- g *Finite Elements Methods Simulations* Simulations for the concentration profiles shown in Fig. 1 b) and c) were conducted with COMSOL Multiphysics. The initial material release is set to be evenly distributed over the whole WE area. Electrolyte mass flow was set to 3 mg/s as measured for the experiments conducted.

## Data Availability

The raw and processed data required to reproduce these findings are available from the corresponding author via [www.repositum.tuwien.ac.at](http://www.repositum.tuwien.ac.at) upon reasonable request.

## Author statement

**Dominik Dworschak:** Methodology, Investigation, Data curation, Writing - original draft, Formal analysis.

**Hsiu-Wei Cheng:** Conceptualization, Validation, Supervision.

**Ching-Shun Ku:** Formal analysis, Visualization.

**Ching-Yu Chiang:** Formal analysis, Visualization.

**Chia-Hsien Lin:** Formal analysis, Visualization.

**Markus Valtiner:** Conceptualization, Validation, Resources, Supervision, Writing - review & editing, Funding acquisition.

## Declaration of Competing Interest

The authors declare that they have no known competing financial interests or personal relationships that could have appeared to influence the work reported in this paper.

## Acknowledgements

The authors acknowledge support by the European Research Council (Grant: CSI.interface, ERC-StG 677663, characterization of surfaces). M. V. gratefully acknowledges support from the K1-COMET center CEST (Centre for Electrochemical Surface Technology, Wiener Neustadt, Project Nr. 865864) funded by the Austrian Research Promotion Agency (FFG). XPS-measurements were carried out with the support of CEITEC Nano Research Infrastructure (ID LM2015041, MEYS CR, 2016-2019),

CEITEC Brno University of Technology. We thank Dr. Hauke Springer for preparing the alloys used (Cr5 and Mo1). We thank Lukas Kalchgruber for finite element based flow simulations of the electrochemical cell used.

## Appendix A. Supplementary data

Supplementary material related to this article can be found, in the online version, at doi:<https://doi.org/10.1016/j.corsci.2021.109629>.

## References

- [1] S.J. Rosenberg, Nickel and Its Alloys, National Bureau of Standards, Washington, 1968.
- [2] A.F. Rowcliffe, L.K. Mansur, D.T. Hoelzer, R.K. Nanstad, Perspectives on radiation effects in nickel-base alloys for applications in advanced reactors, *J. Nucl. Mater.* 392 (2009) 341–352, <https://doi.org/10.1016/j.jnucmat.2009.03.023>.
- [3] M.B. Henderson, D. Arrell, R. Larsson, M. Heobel, G. Marchant, Nickel based superalloy welding practices for industrial gas turbine applications, *Sci. Technol. Weld. Join.* 9 (2004) 13–21, <https://doi.org/10.1179/136217104225017099>.
- [4] S.Y. Persaud, B. Langelier, A. Korinek, S. Ramamurthy, G.A. Botton, R.C. Newman, Characterization of initial intergranular oxidation processes in alloy 600 at a sub-nanometer scale, *Corros. Sci.* 133 (2018) 36–47, <https://doi.org/10.1016/j.corsci.2018.01.020>.
- [5] J.R. Hayes, J.J. Gray, A.W. Szmodis, C.A. Orme, Influence of chromium and molybdenum on the corrosion of nickel-based alloys, *Corrosion* 62 (2006) 491–500, <https://doi.org/10.5006/1.3279907>.
- [6] A.C. Lloyd, J.J. Noël, S. McIntyre, D.W. Shoesmith, Cr, Mo and W alloying additions in Ni and their effect on passivity, *Electrochim. Acta* 49 (2004) 3015–3027, <https://doi.org/10.1016/j.electacta.2004.01.061>.
- [7] N. Ebrahimi, P. Jakupi, J.J. Noël, D.W. Shoesmith, The role of alloying elements on the crevice corrosion behavior of Ni-Cr-Mo alloys, *Corrosion* 71 (2015) 1441–1451, <https://doi.org/10.5006/1848>.
- [8] S.Y. Persaud, R.C. Newman, A review of oxidation phenomena in Ni alloys exposed to hydrogenated steam below 500°C, *Corrosion* 72 (2016) 881–896, <https://doi.org/10.5006/1957>.
- [9] N. Ebrahimi, M.C. Biesinger, D.W. Shoesmith, J.J. Noël, The influence of chromium and molybdenum on the repassivation of nickel-chromium-molybdenum alloys in saline solutions: influence of Cr and Mo on the Repassivation of Ni-Cr-Mo Alloys, *Surf. Interface Anal.* 49 (2017) 1359–1365, <https://doi.org/10.1002/sia.6254>.
- [10] H.-H. Huang, Effect of chemical composition on the corrosion behavior of Ni-Cr-Mo dental casting alloys, *J. Biomed. Mater. Res.* 60 (2002) 458–465, <https://doi.org/10.1002/jbm.10080>.
- [11] J. Zhang, Y. Chen, M.A. Brook, Facile functionalization of PDMS elastomer surfaces using thiol-ene click chemistry, *Langmuir* 29 (2013) 12432–12442, <https://doi.org/10.1021/la403425d>.
- [12] N. Ebrahimi, J.J. Noël, M.A. Rodríguez, D.W. Shoesmith, The self-sustaining propagation of crevice corrosion on the hybrid BCl Ni-Cr-Mo alloy in hot saline solutions, *Corros. Sci.* 105 (2016) 58–67, <https://doi.org/10.1016/j.corsci.2016.01.003>.
- [13] J.D. Henderson, X. Li, D.W. Shoesmith, J.J. Noël, K. Ogle, Molybdenum surface enrichment and release during transpassive dissolution of Ni-based alloys, *Corros. Sci.* 147 (2019) 32–40, <https://doi.org/10.1016/j.corsci.2018.11.005>.
- [14] S. Voyshnis, A. Seyeux, S. Zanna, B. Martin-Cabanac, T. Couvant, P. Marcus, Oxide layer growth on nickel-base alloy surfaces in high temperature water and in O<sub>2</sub> studied by ToF-SIMS with isotopic tracers, *Corros. Sci.* 145 (2018) 212–219, <https://doi.org/10.1016/j.corsci.2018.10.009>.
- [15] A.C. Lloyd, J.J. Noël, D.W. Shoesmith, N.S. McIntyre, The open-circuit ennoblement of alloy C-22 and other Ni-Cr-Mo alloys, *JOM* 57 (2005) 31–35, <https://doi.org/10.1007/s11837-005-0061-x>.
- [16] P. Jakupi, J.J. Noël, D.W. Shoesmith, The evolution of crevice corrosion damage on the Ni-Cr-Mo-W alloy-22 determined by confocal laser scanning microscopy, *Corros. Sci.* 54 (2012) 260–269, <https://doi.org/10.1016/j.corsci.2011.09.028>.
- [17] G. Pajonk, H. Bubert, Influence of pickling high alloyed CrNi-Steels and nickel base alloys with citric acid on the composition of their tarnish oxides, *Microchim. Acta* 133 (2000) 289–293, <https://doi.org/10.1007/s006040070107>.
- [18] X. Li, K. Ogle, The passivation of Ni-Cr-Mo alloys: time resolved enrichment and dissolution of Cr and Mo during passive-active cycles, *J. Electrochem. Soc.* 166 (2019) C3179–C3185, <https://doi.org/10.1149/2.0201911jes>.
- [19] S.O. Klemm, A.A. Topalov, C.A. Laska, K.J. Mayrhofer, Coupling of a high throughput microelectrochemical cell with online multielemental trace analysis by ICP-MS, *Electrochem. Commun.* 13 (2011) 1533–1535, <https://doi.org/10.1016/j.elecom.2011.10.017>.
- [20] A.K. Schuppert, A.A. Topalov, I. Katsounaros, S.O. Klemm, K.J.J. Mayrhofer, A scanning flow cell system for fully automated screening of electrocatalyst materials, *J. Electrochem. Soc.* 159 (2012) F670–F675, <https://doi.org/10.1149/2.009211jes>.
- [21] K. Ogle, S. Weber, Anodic dissolution of 304 stainless steel using atomic emission spectroelectrochemistry, *J. Electrochem. Soc.* 147 (2000) 1770–1780, <https://doi.org/10.1149/1.1393433>.
- [22] M. Volmer, M. Stratmann, H. Viehhaus, Electrochemical and electron spectroscopic investigations of iron surfaces modified with thiols, *Surf. Interface Anal.* 16 (1990) 278–282, <https://doi.org/10.1002/sia.740160158>.
- [23] J.-J. Velasco-Vélez, L.J. Falling, D. Bernsmeier, M.J. Sear, P.C.J. Clark, T.-S. Chan, E. Stotz, M. Hävecker, R. Kraehnert, A. Knop-Gericke, C.-H. Chuang, D.E. Starr, M. Favaro, R.V. Mom, A comparative study of electrochemical cells for in situ x-ray spectroscopies in the soft and tender x-ray range, *J. Phys. D Appl. Phys.* 54 (2021), <https://doi.org/10.1088/1361-6463/abd2ed>, 124003.
- [24] S. Pletincx, S. Abrahami, J. Mol, T. Hauffman, H. Terryn, Advanced (in situ) surface analysis of organic Coating/Metal oxide interactions for corrosion protection of passivated metals. *Encyclopedia of Interfacial Chemistry: Surface Science and Electrochemistry*, Elsevier Science, San Diego, 2018, pp. 1–17.
- [25] M.A. Khillia, H. Mikhail, A. Abu-El Soud, Z.M. Hanafi, Magnetic susceptibility of molybdenum trioxide, dioxide and some suboxides, *Czech J Phys* 30 (1980) 1039–1045, <https://doi.org/10.1007/BF01596177>.
- [26] L. Zha, H. Li, N. Wang, In situ electrochemical study of the growth kinetics of passive film on TC11 alloy in sulfate solution at 300 °C/10 MPa, *Materials* 13 (2020), <https://doi.org/10.3390/ma13051135>.
- [27] L.F. Lin, C.Y. Chao, D.D. Macdonald, A point defect model for anodic passive films: II chemical breakdown and pit initiation, *J. Electrochem. Soc.* 128 (1981) 1194–1198, <https://doi.org/10.1149/1.2127592>.
- [28] N. Cabrera, N.F. Mott, Theory of the oxidation of metals, *Rep. Prog. Phys.* 12 (1949) 163–184, <https://doi.org/10.1088/0034-4885/12/1/308>.
- [29] Z. Wang, E.-M. Paschalidou, A. Seyeux, S. Zanna, V. Maurice, P. Marcus, Mechanisms of Cr and Mo enrichments in the passive oxide film on 316L austenitic stainless steel, *Front. Mater.* 6 (2019) 232, <https://doi.org/10.3389/fmats.2019.00232>.
- [30] R.G. Kelly, J.S. Lee, Localized corrosion: crevice corrosion. *Encyclopedia of Interfacial Chemistry: Surface Science and Electrochemistry*, Elsevier Science, San Diego, 2018, pp. 291–301.
- [31] T. Kaji, T. Sekiai, I. Muto, Y. Sugawara, N. Hara, Visualization of solution chemistry inside crevice by pH and pCl sensing plates, *ECS Trans.* 41 (2019) 205–216, <https://doi.org/10.1149/1.3697590>.
- [32] M. Nie, J.A. Wharton, A. Cranny, N.R. Harris, R.J.K. Wood, K.R. Stokes, Characterisation of crevice and pit solution chemistries using capillary electrophoresis with contactless conductivity detector, *Materials* 6 (2013) 4345–4360, <https://doi.org/10.3390/ma6104345>.
- [33] N. Sridhar, Local corrosion chemistry—a review, *Corrosion* 73 (2017) 18–30, <https://doi.org/10.5006/2246>.
- [34] C. Merola, H.-W. Cheng, D. Dworschak, C.-S. Ku, C.-Y. Chiang, F.U. Renner, M. Valtiner, Nanometer resolved real time visualization of acidification and material breakdown in confinement, *Adv. Mater. Interfaces* 6 (2019), <https://doi.org/10.1002/admi.201802069>, 1802069.
- [35] N.J. Laycock, J. Stewart, R.C. Newman, The initiation of crevice corrosion in stainless steels, *Corros. Sci.* 39 (1997) 1791–1809, [https://doi.org/10.1016/S0010-938X\(97\)00050-4](https://doi.org/10.1016/S0010-938X(97)00050-4).
- [36] N. Sridhar, D.S. Dunn, Effect of applied potential on changes in solution chemistry inside crevices on type 304L stainless steel and alloy 825, *Corrosion* 50 (1994).
- [37] K. Lutton Cwalina, C.R. Demarest, A.Y. Gerard, J.R. Scully, Revisiting the effects of molybdenum and tungsten alloying on corrosion behavior of nickel-chromium alloys in aqueous corrosion, *Curr. Opin. Solid State Mater. Sci.* 23 (2019) 129–141, <https://doi.org/10.1016/j.cossms.2019.03.002>.
- [38] C.R. Clayton, Y.C. Lu, Electrochemical and XPS evidence of the aqueous formation of Mo<sub>2</sub>O<sub>5</sub>, *Surf. Interface Anal.* 14 (1989) 66–70, <https://doi.org/10.1002/sia.740140114>.
- [39] J. Baltrusaitis, B. Mendoza-Sanchez, V. Fernandez, R. Veenstra, N. Dukstiene, A. Roberts, N. Fairley, Generalized molybdenum oxide surface chemical state XPS determination via informed amorphous sample model, *Appl. Surf. Sci.* 326 (2015) 151–161, <https://doi.org/10.1016/j.apsusc.2014.11.077>.
- [40] M.C. Biesinger, B.P. Payne, A.P. Grosvenor, L.W. Lau, A.R. Gerson, R.S. Smart, Resolving surface chemical states in XPS analysis of first row transition metals, oxides and hydroxides: Cr, Mn, Fe, Co and Ni, *Appl. Surf. Sci.* 257 (2011) 2717–2730, <https://doi.org/10.1016/j.apsusc.2010.10.051>.
- [41] K.S. Kim, N. Winograd, X-ray photoelectron spectroscopic studies of nickel-oxygen surfaces using oxygen and argon ion-bombardment, *Surf. Sci.* 43 (1974) 625–643, [https://doi.org/10.1016/0039-6028\(74\)90281-7](https://doi.org/10.1016/0039-6028(74)90281-7).
- [42] A.P. Grosvenor, M.C. Biesinger, R.S. Smart, N.S. McIntyre, New interpretations of XPS spectra of nickel metal and oxides, *Surf. Sci.* 600 (2006) 1771–1779, <https://doi.org/10.1016/j.susc.2006.01.041>.